Topological states and topological phase transition in Cu_2SnS_3 and Cu_2SnSe_3

Liqin Zhou [1,2] Yuting Qian, [1,2] Changming Yue, [3] Yi Jiang [1,2] Zhong Fang, [1,2]
Wei Zhang [4,5,*] Chen Fang [1,2,†] and Hongming Weng [1,2,6,‡]
[1] Beijing National Laboratory for Condensed Matter Physics and Institute of Physics, Chinese Academy of Sciences, Beijing 100190, China
[2] University of Chinese Academy of Sciences, Beijing 100049, China
[3] Department of Physics, University of Fribourg, 1700 Fribourg, Switzerland
[4] Fujian Provincial Key Laboratory of Quantum Manipulation and New Energy Materials, College of Physics and Energy, Fujian Normal University, Fuzhou 350117, China
[5] Fujian Provincial Collaborative Innovation Center for Advanced High-Field Superconducting Materials and Engineering, Fuzhou 350117, China
[6] Songshan Lake Materials Laboratory, Dongguan, Guangdong 523808, China

(Received 19 January 2022; revised 26 April 2022; accepted 24 June 2022; published 22 July 2022)

Based on the first-principles calculations and model analysis, we propose that the isostructural compounds Cu_2SnS_3 and Cu_2SnSe_3 are both the simplest nodal-line semimetals with only one nodal line in their crystal momentum space when spin-orbit coupling (SOC) is ignored. The inclusion of SOC drives Cu_2SnS_3 into a Weyl semimetal (WSM) state with only two pairs of Weyl nodes, the minimum number required for a WSM with time-reversal symmetry. In contrast, SOC leads Cu_2SnSe_3 to a strong topological insulator (STI) state. This difference can be well understood as there is a topological phase transition (TPT). In it, the Weyl nodes are driven by tunable SOC and annihilate in a mirror plane, resulting in a STI. This TPT, together with the evolution of Weyl nodes, the changing of mirror Chern numbers of the mirror plane, and the Z_2 indices protected by time-reversal symmetry, has been demonstrated by the calculation of $Cu_2Sn(S_{1-x}Se_x)_3$ within virtual crystal approximation and an effective $k \cdot p$ model analysis. Though our first-principles calculations have overestimated the topological states in both compounds, we believe that the theoretical demonstration of controlling the TPT and the evolution of Weyl nodes will stimulate further efforts to explore them.

DOI: 10.1103/PhysRevResearch.4.033067

I. INTRODUCTION

After nearly 15 years of development, the classification of topological electronic bands and their topological materials has been quite well developed [1–9]. The gapped states have been classified both with internal and spatial symmetries. The internal symmetries include time-reversal symmetry, chiral (sublattice) symmetry, and particle-hole symmetry, and the spatial symmetries include the crystalline symmetries in all four types of magnetic space groups. The Chern insulator, integer quantum anomalous Hall insulator, topological insulator (TI), topological crystalline insulator (TCI), as well as topological superconductor belong to these classifications. For the metals, the topological classification has been done mainly according to the nodal points close to the Fermi energy. According to the degeneracy, topological charge, and distribution of these nodes, there has been Weyl semimetal (WSM), Dirac semimetal (DSM), topological nodal-line semimetal (TNLS), and multiple-degeneracy nodal point semimetal [10–24]. Topological semimetal phases can be viewed as the intermediate states in the process of the topological phase transition (TPT) between different topological phases, such as the normal insulator (NI) to TI, which has been systematically studied by Murakami *et al.* [25–31]. In inversion-symmetric systems, the conduction band and valence band gradually approach each other in the phase transition process, and the band gap closes at time-reversal invariant momenta (TRIM) only, where a fourfold degenerate Dirac node appears. The intermediate state of the phase transition is a DSM phase, but as a critical point, it is unstable and easy to destroy. On the other hand, for inversion-asymmetric systems, the band gap will close at a certain k point away from TRIM and at least two pairs of Weyl nodes with opposite chirality will emerge as constrained by time-reversal symmetry (TRS) and the no-go theorem. This intermediate state of the phase transition is a WSM phase. The Weyl nodes are separated in reciprocal space and they should appear and disappear in pairs when tuning one or more parameters in the Hamiltonian properly. In this sense, the intermediate WSM phase cannot be destroyed immediately and it is relatively

*zhangw721@163.com
†cfang@iphy.ac.cn
‡hmweng@iphy.ac.cn

robust against perturbation, facilitating the material realization.

Recently, Lohani *et al.* prepared ordered and disordered polymorphic samples of Cu_2SnS_3 present in the space groups Cc and $F\bar{4}3m$, respectively, and studied their electronic and vibrational properties systematically by experiments and *ab initio* calculations [32]. In this work, we have theoretically investigated two isostructural compounds Cu_2SnS_3 and Cu_2SnSe_3 belonging to the space group $Imm2$ [33–35]. We find that they are very suitable to study the TPT from a WSM to a TI. When spin-orbit coupling (SOC) is ignored, both of them are a nodal-line semimetal with only one nodal ring around the Fermi energy lying in one mirror plane. When SOC is considered, Cu_2SnS_3 becomes a WSM with two pairs of Weyl nodes, while Cu_2SnSe_3 is a strong TI. The evolution and annihilation of Weyl nodes in these isostructural and isoelectronic family compounds can be demonstrated by systematically tuning the effective SOC. To do this, we employ the virtual crystal approximation (VCA) method to simulate the different Se doping concentrations of $Cu_2Sn(S_{1-x}Se_x)_3$. Since there are no topologically nontrivial symmetry-based indicators in their space group $Imm2$ (No. 44) to directly judge their topological classification [2,36,37], we characterize their topological states by calculating the mirror Chern number (MCN) for two mutually perpendicular mirror planes and Z_2 indices according to the Wilson-loop method [38,39]. To reveal the mechanism of TPT, an effective $k \cdot p$ model has been constructed and analyzed according to the representations of the bands forming the nodal ring. In the following, we first introduce the calculation method, and then discuss the topological states of Cu_2SnS_3 and Cu_2SnSe_3 without and with SOC, respectively. Finally, the TPT from the WSM in Cu_2SnS_3 to the TI of Cu_2SnSe_3 has been systematically investigated.

II. METHOD

The density functional theory (DFT) calculation of the electronic structures for Cu_2SnS_3 and Cu_2SnSe_3 is performed by using the Vienna *ab initio* simulation package (VASP) [40]. The generalized gradient approximation (GGA) with the Perdew-Burke-Ernzerhof (PBE) functional is selected to describe the exchange-correlation energy [41,42]. The cutoff energy for the plane-wave basis is set to 520 eV and the reciprocal space is sampled by a $11 \times 11 \times 11$ Γ − centered$k$ mesh. To further calculate the topological properties of Cu_2SnS_3 and Cu_2SnSe_3 such as surface states and MCN, we have constructed the tight-binding model with the maximally localized Wannier functions (MLWF) [43] generated for Cu $3d$, Sn $5s + p$, and S (Se) $3p$ ($4p$) orbitals. The surface states and Fermi arcs are calculated using the WANNIERTOOLS package [44], which is based on the surface Green's function method. In order to study the TPT process between Cu_2SnS_3 and Cu_2SnSe_3, we use the VCA method (suppose different proportions of S and Se atoms simultaneously occupy the same atomic sites) to calculate the band structures with different S:Se ratios. Similarly, we linearly mix the above tight-binding Hamiltonian based on Wannier functions of the two parent compounds to obtain the Hamiltonian of the doped one, which is found to be efficient in further determining the phase transition critical point and the evolution of the Weyl points.

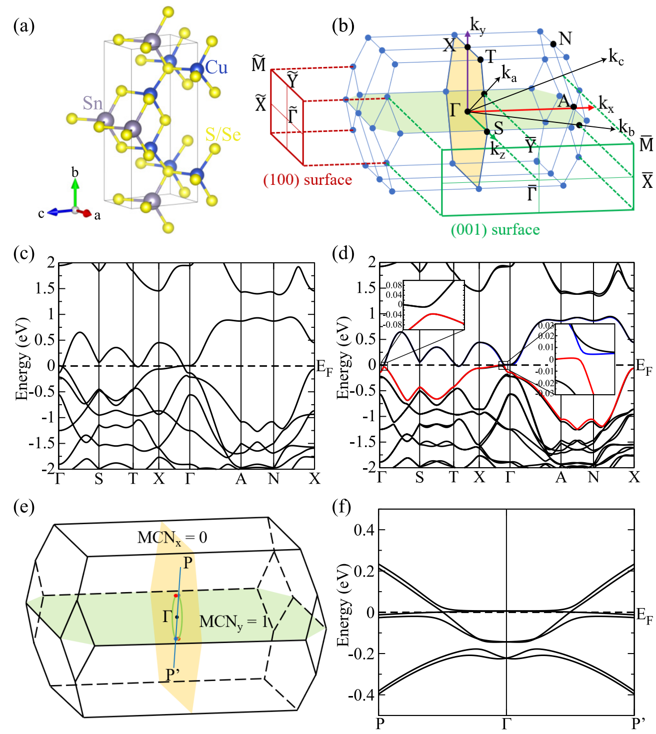

FIG. 1. (a) The crystal structure of $Cu_2SnS_3(Se_3)$. The blue, gray, and yellow balls represent Cu, Sn, and S (Se) atoms, respectively. (b) The bulk BZ and the projected surface BZ for (001) and (100) surfaces. The light yellow and light green planes represent M_x and M_y planes, respectively. (c),(d) The band structures of Cu_2SnS_3 without and with SOC, respectively. (e) Three-dimensional (3D) schematic diagram of the nodal ring (in the absence of SOC) and Weyl points (with SOC) in the BZ. The green line represents the nodal ring. The blue and red dots denote the Weyl points with opposite chirality. (f) The band along the path passing through two Weyl points with the same chirality related with time-reversal symmetry. The path P to P' is shown in (e).

III. RESULTS AND DISCUSSIONS

The crystal structure and Brillouin zone (BZ) of Cu_2SnS_3 and Cu_2SnSe_3 are shown in Figs. 1(a) and 1(b). They belong to the same space group $Imm2$ (No. 44), which includes two mirror reflection symmetries M_x and M_y perpendicular to the x and y axis, respectively, and one twofold rotation symmetry C_{2z} along the z axis. It has time-reversal symmetry (TRS) T but no inversion symmetry, which means the minimum number of Weyl nodes is four, with two pairs in opposite chirality.

A. Cu_2SnS_3

The band structure of Cu_2SnS_3 calculated without SOC is shown in Fig. 1(c). The two mirror reflection symmetries M_x and M_y are represented by the colored planes in Fig. 1(b). We can clearly find the band crossing between the highest valence band and the lowest conduction band along the Γ-S and X-Γ directions. According to the representation analysis of the symmetric operations, the conduction band and valence band forming the crossing node on path Γ-S have opposite eigenvalues of the M_x and C_{2z} operators, but the same eigenvalues of the M_y operator. This means that the band crossing is protected by the M_x and C_{2z} symmetries. The crossing point on the path X-Γ is also protected by the M_x symmetry. By searching the entire BZ, we find that these band-crossing points form a closed nodal ring around Γ on the M_x plane, as shown in Fig. 1(e). Therefore, without SOC, Cu_2SnS_3 is the simplest TNLS with only one nodal ring.

When SOC is taken into account, the crossing points on the above-mentioned nodal ring are fully gapped. The band structure near the Fermi level is plotted in Fig. 1(d). However, there are two pairs of Weyl points created at the generic momenta on the $k_z = 0$ plane. They are symmetric about the M_x and M_y planes. They also respect the C_{2z} rotation symmetry and TRS T. It is noted that the $k_z = 0$ plane is invariant under the joint operation $C_{2z} * T$, which results in a zero or π Berry phase for any loop in this plane [7,31]. The positions and chiralities of the Weyl nodes are shown in Fig. 1(e). The bands along the k path, which connects a pair of Weyl points with the same chirality to the Γ point, have been plotted in Fig. 1(f). The energy of the Weyl points is very close to the Fermi level, being about 1.4 meV above it.

It is noted that there is no topological indicator [2,36,37] that can be used to determine the topological classification in space group No. 44. Furthermore, spatial inversion symmetry is also absent so that the Fu-Kane parity formula [45–47] is not applicable. To determine its topological phase, we take the Wilson-loop method to calculate the Z_2 invariant protected by TRS T and the MCNs of the mirror planes [17,38]. The MCN calculations for the two mirror planes are plotted in Figs. 2(a) and 2(b). They clearly show that MCN = 0 for the M_x plane, while MCN = 1 for the M_y plane. To verify the results, we further calculate the flow of Wannier centers of all occupied states along half of the reciprocal lattice vector in the M_x and M_y planes, which can give out a Z_2 invariant protected by TRS. As shown in Figs. 2(c) and 2(d), Z_2 is 0 for the $k_x = 0$ plane, while it is 1 for the $k_y = 0$ plane, which is consistent with the MCN results. The existence of Weyl nodes between two nonparallel mirror planes with different MCNs was first pointed out and demonstrated in TaAs [17], and their influence on the pattern of Fermi arcs has also been discussed and studied experimentally in TaAs [48]. Therefore, the net topological charge of the Weyl nodes in one of the four blocks divided by these two mirror planes should be an odd number. In addition, the $k_z = 0$ plane is invariant under the joint operation of $C_2 * T$. Thus, there must be Weyl nodes in this plane, which is essentially the same as the constraint of in-plane Weyl nodes in the inversion-symmetric magnetic space group with odd Z_4 invariant and joint $C_2 * T$ symmetry [7,31].

The surface states and Fermi arcs of Cu_2SnS_3 on the (100) and (001) projected surfaces are plotted in Figs. 2(e)–2(h). On the (001) surface, four Weyl points are all projected onto the surface separately. There are two Fermi arcs connecting the two pairs of Weyl points, respectively, which is clearly observed in the enlarged illustration of Fig. 2(f). The $\bar{\Gamma}$ - $\bar{Y}$ and $\bar{\Gamma}$ - $\bar{X}$ lines are the projection of the M_x and M_y plane, respectively. Along the $\bar{\Gamma}$ - $\bar{X}$ line, we can find a cross where

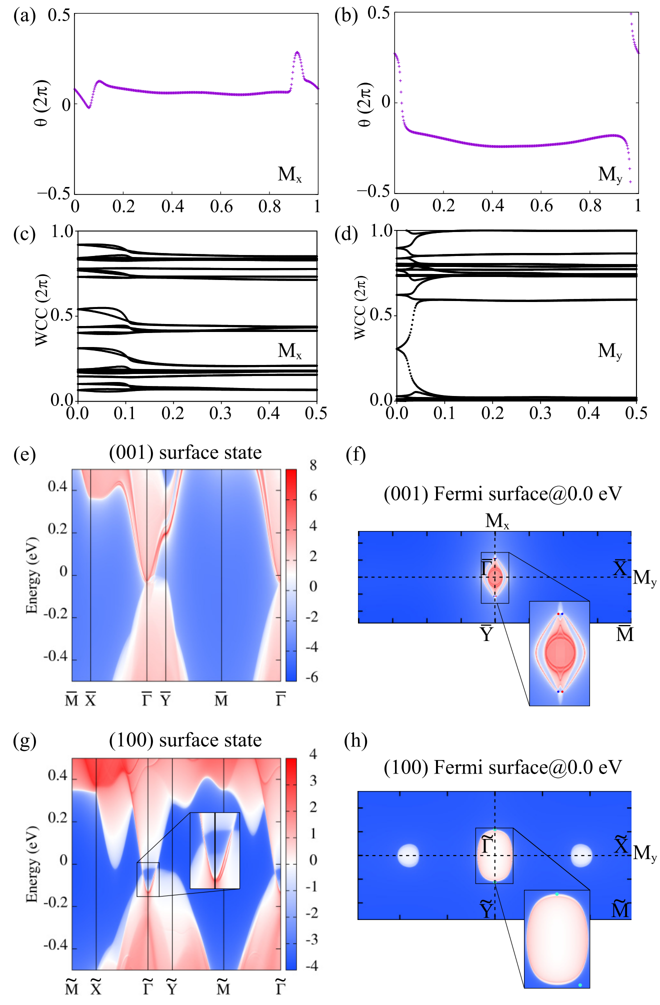

FIG. 2. The calculated topological properties of Cu_2SnS_3. (a),(b) The flow chart of the average position of the Wannier centers for occupied bands with mirror eigenvalue $+i$ in the (a) M_x and (b) M_y planes. (c),(d) The flow chart of the Wannier centers for all occupied bands in the (c) M_x and (d) M_y planes across half of the reciprocal lattice vector. (e) The surface states of the (001) surface and (f) the corresponding Fermi surface. (g) The surface states of the (100) surface and (h) the corresponding Fermi surface. The red and blue dots are the projections of opposite chiral Weyl points, respectively. The cyan dots are the superposition of two projected Weyl points with opposite chirality.

the Fermi arc runs through it, which comes from MCN = 1 for the M_y plane. There is no Fermi arc crossing the $\bar{\Gamma}$ - $\bar{Y}$ line since MCN = 0 for the M_x plane. It is noted that if the Weyl nodes are off the $k_z = 0$ plane, the number of Weyl nodes will be doubled and two Weyl nodes of the same chirality will be superposed on each other when projected onto the (001) surface. The number of Fermi arcs connecting each projection should be two. The different MCNs for the M_x and M_y planes limit that there must be an odd number of Fermi arcs crossing $\bar{\Gamma}$ - $\bar{X}$ and an even number of Fermi arcs crossing $\bar{\Gamma}$ - $\bar{Y}$. Therefore, there is no way to satisfy all these constraints if assuming the Weyl nodes were off the $k_z = 0$ plane.

On the (100) surface, two opposite chiral Weyl nodes are projected to the same point on the $\tilde{\Gamma}$ - $\tilde{Y}$ line, as shown in

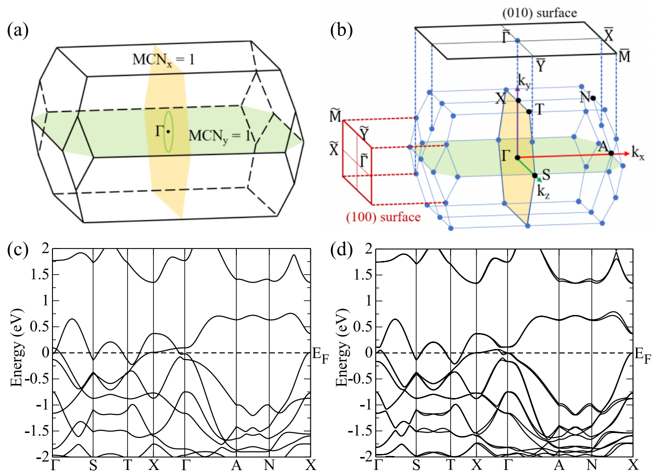

FIG. 3. (a) 3D schematic diagram of the nodal ring for Cu_2SnSe_3 in the absence of SOC. (b) The bulk BZ and the projected surface BZ for (010) and (100) surfaces. (c),(d) The band structures of Cu_2SnSe_3 without and with SOC, respectively.

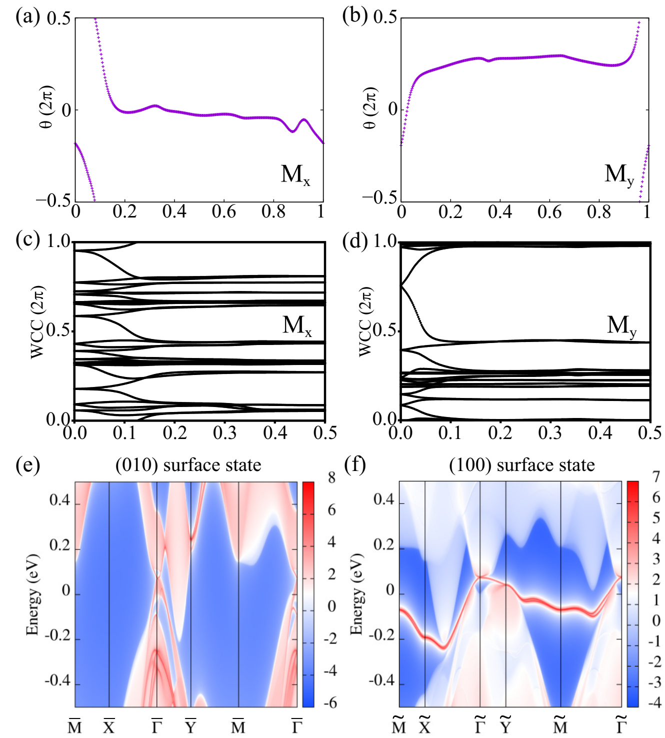

FIG. 4. The calculation results of the topological properties of Cu_2SnSe_3. (a),(b) The flow chart of the average position of the Wannier centers obtained by the Wilson-loop calculation for bands with mirror eigenvalue i in the (a) M_x and (b) M_y planes. (c),(d) The flow chart of the Wannier centers of all occupied states in the (c) M_x and (d) M_y planes along half of the reciprocal lattice vector. (e),(f) The surface states of the (010) projected surface and (100) projected surface, respectively.

Fig. 2(h). Therefore, each projective point should be connected by two or zero Fermi arcs. Here, the $\tilde{\Gamma}$ - $\tilde{X}$ line is the projection of the M_y plane. We can still find that one Fermi arc sticking close to the bulk state crosses this line, which is consistent with MCN = 1 for the M_y plane. In Fig. 2(g), the projected bulk Weyl points form solid Dirac cones with continuous eigenenergies along $\tilde{\Gamma}$ - $\tilde{Y}$. The surface states form an empty Dirac cone and have the Dirac node at $\tilde{\Gamma}$. Along $\tilde{\Gamma}$ - $\tilde{Y}$, both of its two branches merge into the solid Dirac cone where the bulk Weyl nodes are projected. Along $\tilde{\Gamma}$ - $\tilde{X}$, there is only one branch connecting the bulk conduction bands and the other one merges into the valence states, which is consistent with MCN = 1 for M_y.

B. Cu_2SnSe_3

The band structures of Cu_2SnSe_3 without and with SOC are shown in Fig. 3(c) and 3(d), respectively. In the absence of SOC, Cu_2SnSe_3 is also a nodal-line semimetal with only one nodal ring centering at Γ in the M_x plane. However, when SOC is taken into account, the band structure of Cu_2SnSe_3 is fully gapped at each k point along the nodal line. It can be looked at as an insulator, although there is no global gap in the whole BZ.

In order to determine whether it is a topologically nontrivial insulator, we further obtain the MCNs for the M_x and M_y planes, as shown in Figs. 4(a) and 4(b). It is obvious that MCN = 1 for both of M_x and M_y planes, consistent with the Z_2 invariant calculation shown in Figs. 4(c) and 4(d). Thus, Cu_2SnSe_3 might be a WSM with an even number of Weyl nodes in one-quarter of the BZ divided by the M_x and M_y planes, or a strong TI with Z_2 indices (1;000). We have found that the former situation is possible in another family member compound Cu_2GeSe_3, as shown in the Appendix. The present compound Cu_2SnSe_3 is the latter case. The most typical feature of a TI is the appearance of an odd number of Dirac cones on their surfaces. We further calculate the (010) and (100) surface states of Cu_2SnSe_3, as shown in Figs. 4(e) and 4(f). There is one Dirac cone at the $\tilde{\Gamma}$ point on either the (010) or (100) surface and the two branches of the Dirac cone connecting the valence and conduction bands, respectively.

IV. TOPOLOGICAL PHASE TRANSITION

As the materials of a family with the same space group, Cu_2SnS_3 and Cu_2SnSe_3 are both topological nodal ring semimetals when SOC is not taken into account, but they are obviously different in band topology when SOC is considered. It is intriguing to understand the mechanism underlying this difference. Therefore, we are going to explore the process of TPT between them continuously from a WSM to a TI by doping Se into Cu_2SnS_3, through which the strength of the SOC can be tuned.

We use the virtual crystal approximation (VCA) method to calculate the bands of $Cu_2Sn(S_{1-x}Se_x)_3$ to simulate the Se doping effect, as shown in Figs. 5(a)–5(d). The change in lattice constants is linearly scaled between Cu_2SnS_3 and Cu_2SnSe_3 with the doping concentration. We note that experimentally, the doping of Se into Cu_2SnS_3 has been done [49] and we have also estimated the formation energy of several doping concentrations, as shown in Appendix E. It can be seen that the band inversion between the valence band and the conduction band around Γ remains as the Se doping ratio increases from Fig. 5(a) to Fig. 5(d), and the spin splitting

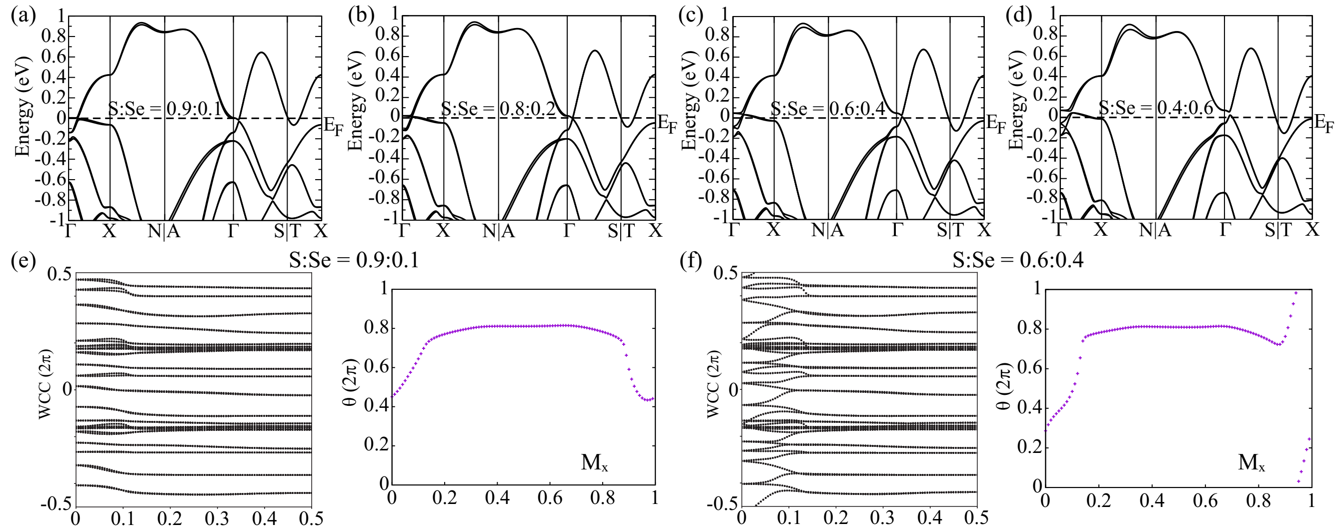

FIG. 5. (a)–(d) Band structures calculated by the VCA method with different values of the S:Se ratio. (e),(f) The flow of Wannier centers and mirror Chern numbers of the M_x plane with different S:Se ratio values.

in these bands also increases due to enhanced SOC. This indicates that the SOC is tunable. In order to accurately determine where the phase transition has occurred, we calculated the MCN and Z_2 for the M_x plane in different doping cases. We find that when S:Se $= 0.9$:0.1, the MCN and Z_2 on the M_x plane are both zero. When S:Se $= 0.6$:0.4, both the MCN and Z_2 on the M_x plane become one, as shown in Figs. 5(e) and 5(f), indicating that a TPT has occurred around this point.

This work presents a simple and ideal model material system for realizing the TPT in a 3D case with TRS as proposed by Murakami [28]. The TPTs in other situations, such as those in different dimensions [50,51] and those driven by changes of crystal structure [52] and magnetism [31,53], have also been studied. The process of Weyl nodes annihilation in a pair and the TPT from a WSM to a TI are shown in Fig. 6(a). This is further simulated by using the linear mixing of the tight-binding Hamiltonians of Cu_2SnS_3 and Cu_2SnSe_3 constructed from the generated Wannier functions. We find that the Weyl points gradually approach the $k_x = 0$ plane along the trajectory when the Se doping ratio increases, as shown in Fig. 6(b). According to the results, we find that at about S:Se $= 0.63$:0.37, the Weyl points finally annihilate on the $k_x = 0$ plane, and a TPT from a WSM to a TI is realized with the MCN $= 0$ for M_x. The critical value of S:Se determined from linear mixing of the tight-binding Hamiltonian is nearly the same as the first-principles calculation within VCA.

In order to further understand the TPT, we first construct a two-band $k \cdot p$ model, which describes the nodal ring around the Γ point without SOC. The Γ point has little-group symmetries M_x, M_y, and C_{2z}, and time reversal T. According to the band representations, we can obtain the operator $M_x = \tau_z$, $M_y = \tau_0, C_{2z} = \tau_z, T = K$, where K is the complex conjugate operator. The Hamiltonian expanded around the Γ point with momentum $\mathbf{q} = (q_x, q_y, q_z)$ can be simply written as

$$H_0(\mathbf{q}) = (m - \mathbf{q}^2)\tau_z + 2q_x\tau_y. \quad (1)$$

In the absence of SOC, the Hamiltonian forms a closed nodal ring around Γ with radius m on the $k_y - k_z$ plane when $m > 0$. When $m < 0$, the nodal ring disappears and the system becomes trivial. In the following, we always assume $m > 0$.

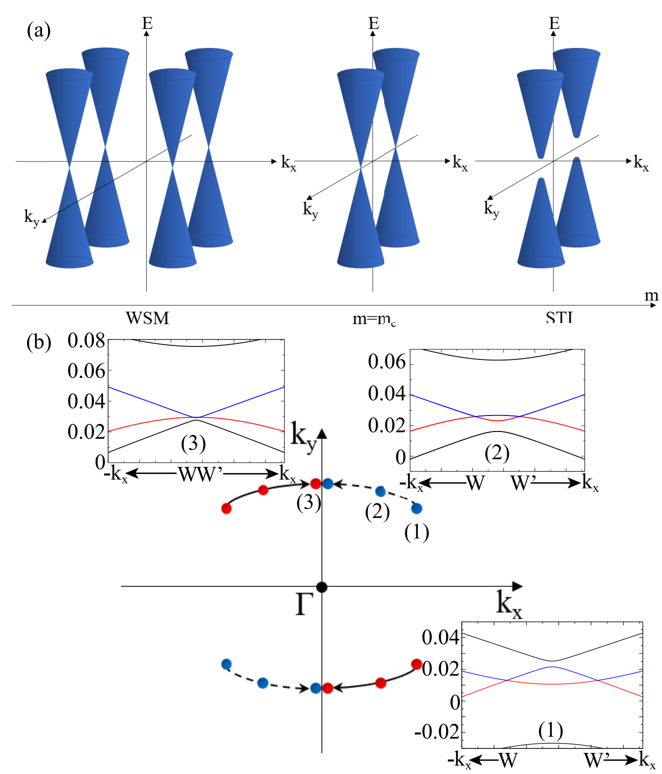

FIG. 6. (a) Schematic evolution of the topological phase transition from Cu_2SnS_3 (WSM) to Cu_2SnSe_3 (strong topological insulator, STI). (b) Band structures of $Cu_2Sn(S_{1-x}Se_x)_3$ calculated by linear mixing of Wannier Hamiltonians with Se doping of 0.0 (1), 0.3 (2), and 0.365 (3). The k path passes through the two Weyl points with opposite chirality along the k_x axis.

When SOC is included, the two-band $k \cdot p$ model should become a four-band model because of the spin degree of freedom. The matrix representations of the M_x, M_y, C_{2z}, and T symmetries can be obtained:

$$M_x = i\tau_z \otimes s_x, M_y = i\tau_0 \otimes s_y, C_{2z} = i\tau_z \otimes s_z, T = i\tau_0 \otimes s_y K. \tag{2}$$

By considering the symmetry constraints cast by M_x, M_y, C_{2z}, and T, all symmetry-allowed $k \cdot p$ terms can be obtained [54,55], and we choose the following form of the $k \cdot p$ Hamiltonian with extra mass term m_1 in order to describe the TPT:

$$H(\mathbf{q}) = (m - \mathbf{q}^2)\tau_z s_0 + 2q_x\tau_y s_0 + q_y\tau_x s_z + q_z\tau_x s_y + m_1\tau_y s_y. \tag{3}$$

For the M_x plane, by applying the unitary matrix U diagonalized M_x operator to $H(q_x = 0)$, we can get the block diagonal matrix of $H(q_y, q_z)$ in the i or $-i$ eigenvalue subspaces of M_x [56,57],

$$UM_xU^{-1} = \begin{pmatrix} i & 0 & 0 & 0 \\ 0 & i & 0 & 0 \\ 0 & 0 & -i & 0 \\ 0 & 0 & 0 & -i \end{pmatrix}, \tag{4}$$

$$UH(q_y, q_z)U^{-1} = \begin{pmatrix} q_y^2 + q_z^2 - m & -q_y + iq_z - m_1 & 0 & 0 \\ -q_y - iq_z - m_1 & -q_y^2 - q_z^2 + m & 0 & 0 \\ 0 & 0 & q_y^2 + q_z^2 - m & -q_y - iq_z + m_1 \\ 0 & 0 & -q_y + iq_z + m_1 & -q_y^2 - q_z^2 + m \end{pmatrix}. \tag{5}$$

The subspace Hamiltonian of the $\pm i$ eigenvalue is

$$H_{yz}^{\pm i}(\mathbf{q}) = \mathbf{d} \cdot \boldsymbol{\sigma} = (-q_y \mp m_1)\sigma_x \mp q_z\sigma_y + \left(q_y^2 + q_z^2 - m\right)\sigma_z, \tag{6}$$

and the MCN on the M_x plane can be calculated by

$$C_{M_x}^{\pm i} = -\frac{1}{4\pi}\int dq_y dq_z \widehat{\mathbf{d}} \cdot (\partial_{q_y}\widehat{\mathbf{d}} \times \partial_{q_z}\widehat{\mathbf{d}}), \tag{7}$$

where $\widehat{\mathbf{d}} = \mathbf{d}/|\mathbf{d}|$. We find that when $m_1^2 < m$, $C_{M_x} = 1$; and when $m_1^2 > m$, $C_{M_x} = 0$.

For the M_y plane, we can obtain the matrix of $H(q_x, q_z)$ by applying the unitary matrix U' diagonalized M_y operator to $H(q_y = 0)$:

$$U'H(q_x, q_z)U'^{-1} = \begin{pmatrix} q_x^2 + q_z^2 - m & 2iq_x + q_z + im_1 & 0 & 0 \\ -2iq_x + q_z - im_1 & -q_x^2 - q_z^2 + m & 0 & 0 \\ 0 & 0 & q_x^2 + q_z^2 - m & 2iq_x - q_z - im_1 \\ 0 & 0 & -2iq_x - q_z + im_1 & -q_x^2 - q_z^2 + m \end{pmatrix}. \tag{8}$$

The subspace Hamiltonian of the $\pm i$ eigenvalue is

$$H_{xz}^{\pm i}(\mathbf{q}) = \mathbf{d} \cdot \boldsymbol{\sigma} = \pm q_z\sigma_x + (-2q_x \mp m_1)\sigma_y + \left(q_x^2 + q_z^2 - m\right)\sigma_z, \tag{9}$$

and the MCN on the M_y plane can be calculated by

$$C_{M_y}^{\pm i} = -\frac{1}{4\pi}\int dq_x dq_z \widehat{\mathbf{d}} \cdot (\partial_{q_x}\widehat{\mathbf{d}} \times \partial_{q_z}\widehat{\mathbf{d}}). \tag{10}$$

We find that when $m_1^2 < 4m$, $C_{M_y} = 1$; and when $m_1^2 > 4m$, $C_{M_y} = 0$.

Therefore, we can find that when $m_1^2 > 4m$, the MCNs on the M_x and M_y planes are both 0. When $m < m_1^2 < 4m$, the MCNs change to $C_{M_x} = 0$ and $C_{M_y} = 1$, with two pairs of Weyl points emerging on the $k_z = 0$ plane with coordinate $(\pm\sqrt{(m_1^2 - m)/3}, \pm\sqrt{(4m - m_1^2)/3}, 0)$, which corresponds to the case of the Weyl semimetal Cu_2SnS_3. When $m_1^2 < m$, the Weyl points are pairwise annihilated on the k_y axis, and the MCNs both become 1, which corresponds to the case of STI Cu_2SnSe_3. The detailed phase diagram is shown in Fig. 7.

V. SUMMARY

Through first-principles calculations, we have proposed that Cu_2SnS_3 and Cu_2SnSe_3 can be used to model the topological phase transition from a WSM to a TI. In the absence of SOC, both of them are the simplest nodal-line semimetal with only a single nodal ring centering at Γ, which is protected by M_x symmetry and lies in the mirror plane. When SOC is taken into account, they are quite different. For Cu_2SnS_3, the

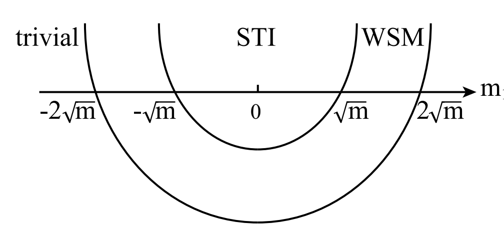

FIG. 7. The schematic phase diagram of topological phase transitions between the trivial insulator, Weyl semimetal, and STI by adjusting parameter m_1 when $m > 0$.

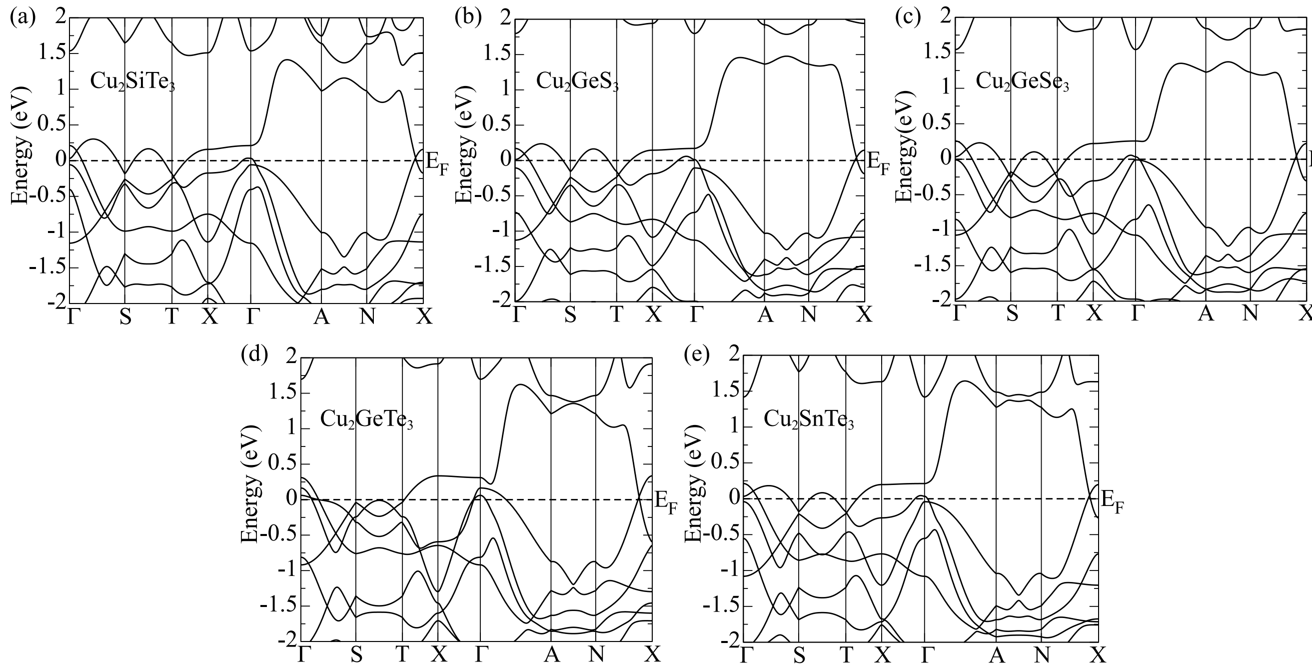

FIG. 8. Band structures of Cu_2SiTe_3, Cu_2GeS_3, Cu_2GeSe_3, Cu_2GeTe_3, and Cu_2SnTe_3 along high-symmetry points without the spin-orbit coupling.

nodal ring evolves into two pairs of Weyl points in the $k_z = 0$ plane, as indicated by the different MCN for the M_x and M_y planes, namely, MCN = 0 for the M_x plane and MCN = 1 for the M_y plane. For Cu_2SnSe_3, the nodal ring is fully gapped and the system becomes a strong TI, as indicated by the same MCN = 1 for both the M_x and M_y planes. The difference in them comes from the different strength of the effective SOC, which can be systematically tuned by doping Se into Cu_2SnS_3. Employing VCA, we have simulated the doping concentration continuously to show the movement of Weyl points and their annihilation in the M_x plane during the TPT. The critical doping level is S:Se = 0.63:0.37. We have also constructed a $k \cdot p$ model to explain these results. Here, it must be noted that all the above results on specific materials are based on the GGA calculations, which usually overestimate the band inversion. The previous work [33–35] mentioned

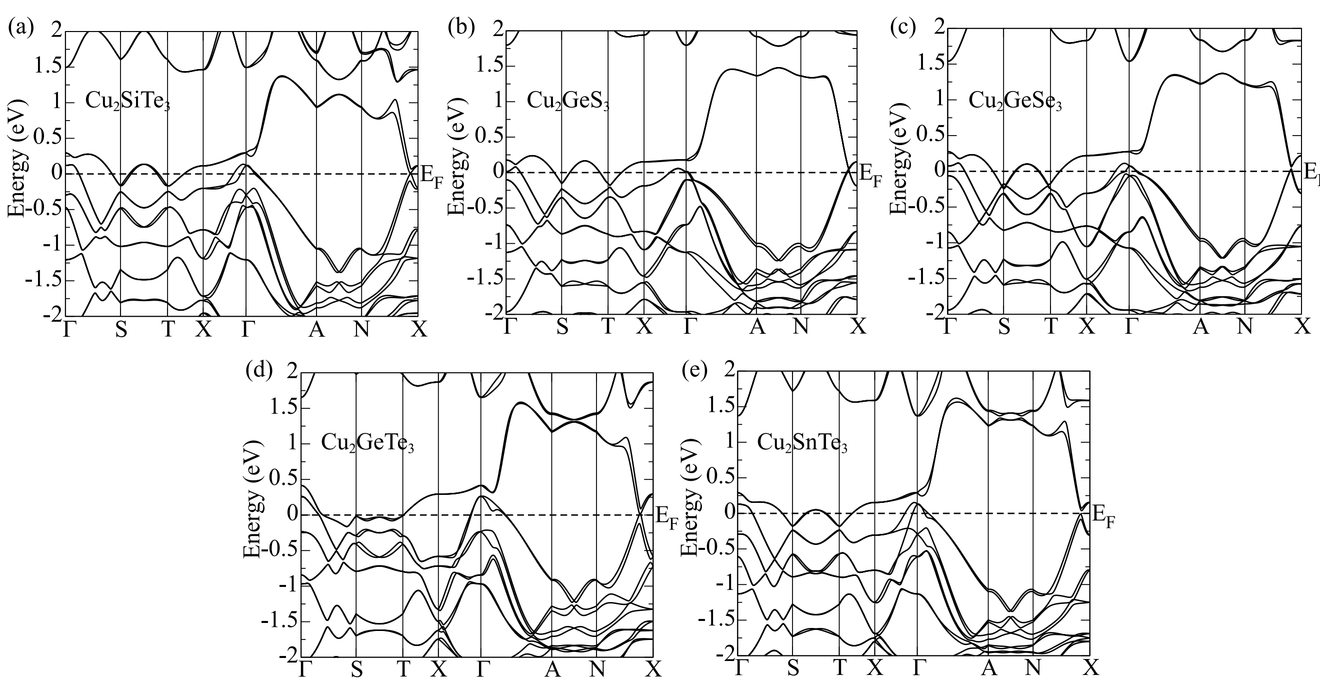

FIG. 9. Band structures of Cu_2SiTe_3, Cu_2GeS_3, Cu_2GeSe_3, Cu_2GeTe_3, and Cu_2SnTe_3 along high-symmetry points with the spin-orbit coupling.

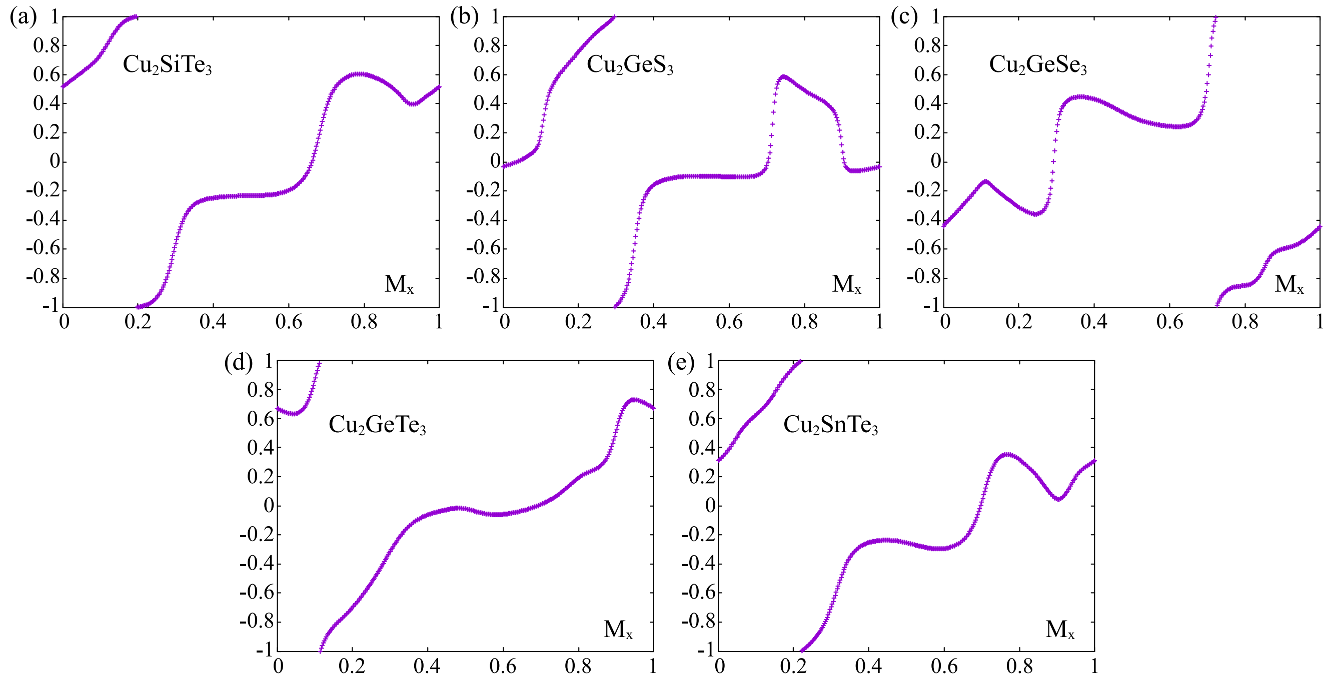

FIG. 10. Mirror Chern numbers (MCNs) of Cu_2SiTe_3, Cu_2GeS_3, Cu_2GeSe_3, Cu_2GeTe_3 and Cu_2SnTe_3 for the M_x plane.

that Cu_2SnS_3 and Cu_2SnSe_3 are gapped insulators in reality and our improved hybrid functional (HSE06) calculations, shown in the Appendix, are consistent with them. There are still some family compounds, such as Cu_2SiTe_3, Cu_2GeSe_3, Cu_2GeTe_3, and Cu_2SnTe_3, that keep the band inversion, and their band topology can be analyzed similarly. Nevertheless, our work is of importance and is useful to theoretically study the topological states and phase transitions among them.

ACKNOWLEDGMENTS

We acknowledge the support from the National Natural Science Foundation (Grants No. 11925408, No. 11974076, No. 11921004, and No. 12188101), the Ministry of Science and Technology of China (Grant No. 2018YFA0305700), the Chinese Academy of Sciences (Grant No. XDB33000000), the K. C. Wong Education Foundation (Grant No. GJTD-2018-01), the Beijing Natural Science Foundation (Grant No.

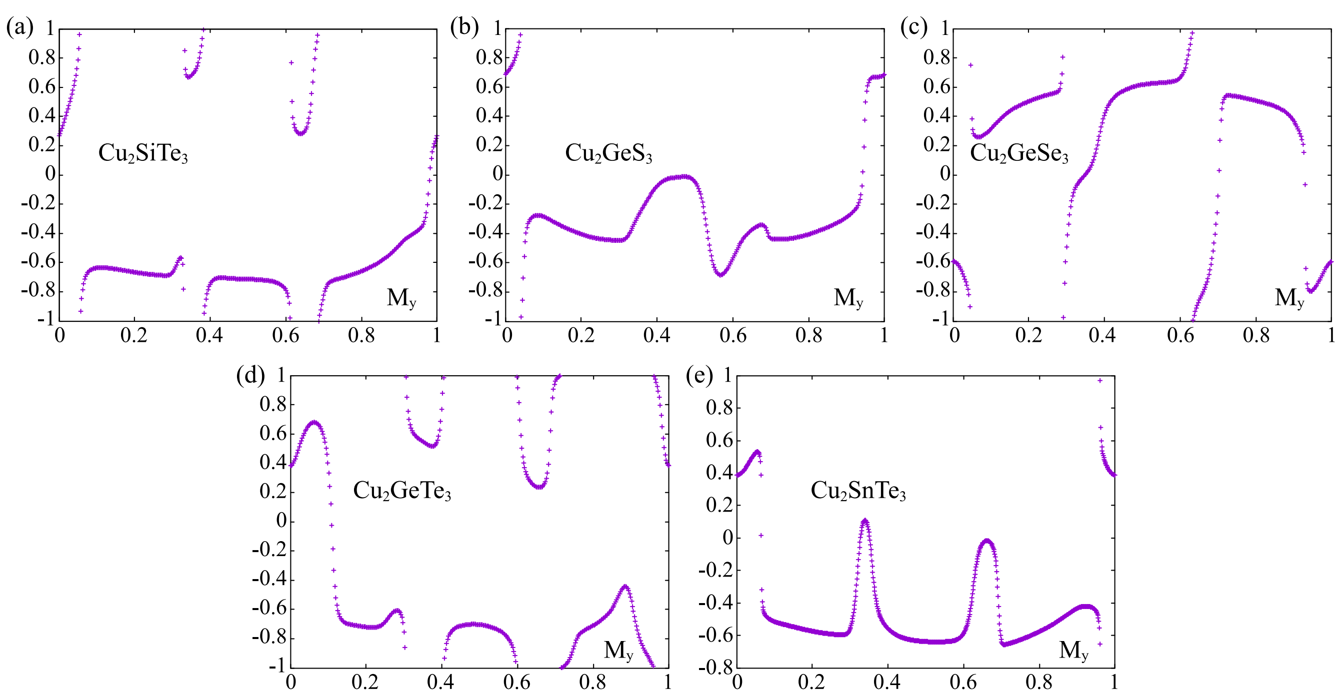

FIG. 11. Mirror Chern numbers (MCNs) of Cu_2SiTe_3, Cu_2GeS_3, Cu_2GeSe_3, Cu_2GeTe_3 and Cu_2SnTe_3 for the M_y plane.

TABLE I. The distribution of Weyl points in the Cu_2SnS_3 family.

Material	a (Å)	b (Å)	c (Å)	Weyl points (k_x, k_y, k_z) ($2\pi/ita$)	Energy (eV)	Number
Cu_2SiTe_3	4.2527	12.5882	5.9446	Upper and lower surfaces of BZ		8 small nodal-rings
Cu_2GeS_3	3.7660	11.3210	5.2100	(0.0510, 0.4044, 0.3047)	–0.0749	8
				(0.0287, 0.2935, 0.2154)	0.0062	8
Cu_2GeSe_3	3.9600	11.8600	5.4850	(0.0617, 0.3173, 0.2536)	–0.0111	8
Cu_2GeTe_3	4.2115	12.6410	5.9261	(0.1313, 0.0775, 0.1327)	0.1290	8
				Upper and lower surfaces of BZ		4 large nodal-rings
Cu_2SnS_3	3.8937	11.5720	5.4436	(0.0061, 0.1120, 0.0000)	0.0014	4
Cu_2SnSe_3	4.1158	12.2715	5.7528	Topological insulator (TI)		0
Cu_2SnTe_3	4.2740	12.8330	6.0430	(0.0576, 0.1502, 0.1226)	0.0748	8
				(0.0782, 0.4763, 0.3110)	–0.1824	8

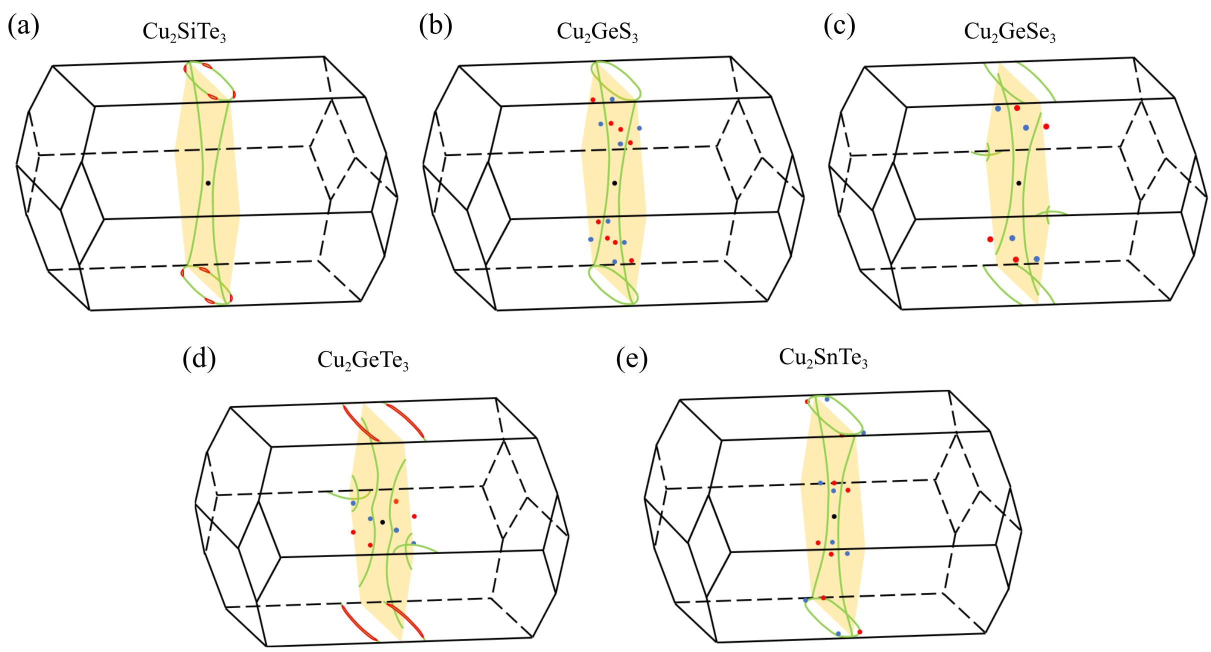

FIG. 12. The schematic diagrams of the Weyl points distribution of Cu_2SiTe_3, Cu_2GeS_3, Cu_2GeSe_3, Cu_2GeTe_3, and Cu_2SnTe_3. The green line represents the nodal chain and nodal ring. The blue dots denote the Weyl points with negative chirality and the red dots denote the Weyl points with positive chirality.

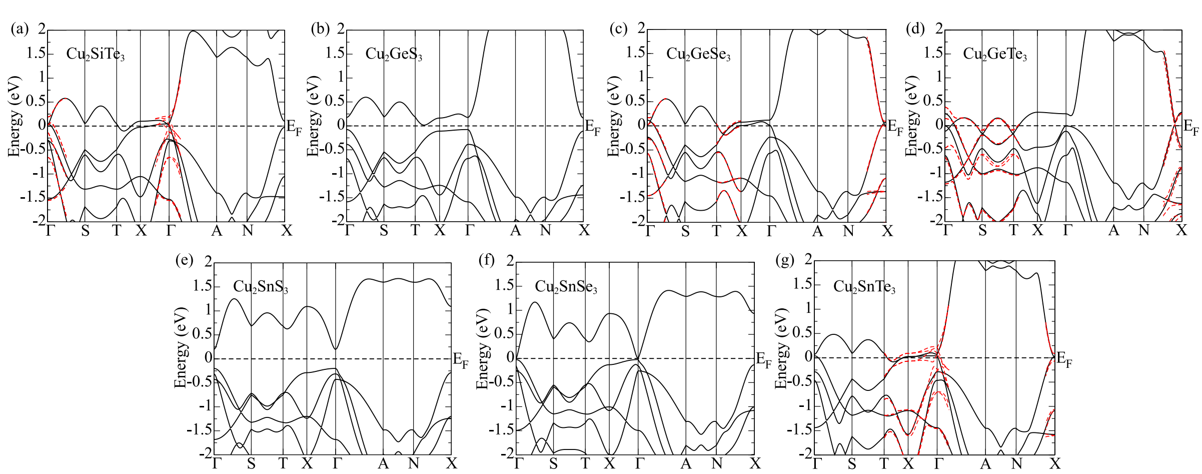

FIG. 13. The band structures of Cu_2SiTe_3, Cu_2GeS_3, Cu_2GeSe_3, Cu_2GeTe_3, Cu_2SnS_3, Cu_2SnSe_3, and Cu_2SnTe_3 with HSE06 along high-symmetry points without the spin-orbit coupling. The red dotted lines in part of the figures are the bands with SOC for comparison.

Z180008), and the Beijing Municipal Science and Technology Commission (Grant No. Z191100007219013). C.Y. is supported by the Swiss National Science Foundation (Grant No. 200021-196966). W.Z. is supported by the Key Project of Natural Science Foundation of Fujian Province (Grant No. 2021J02012).

APPENDIX A: BAND STRUCTURES OF THE OTHER MEMBERS IN Cu_2SnS_3 FAMILY

In this Appendix, we present, in Figs. 8 and 9, the bulk band structures of the other members in the Cu_2SnS_3 family without and with spin-orbit coupling (SOC), which are all calculated using the GGA.

APPENDIX B: MCNs OF M_x AND M_y PLANES FOR OTHER MATERIALS OF Cu_2SnS_3 FAMILY

In this Appendix, we give, in Figs. 10 and 11, the MCNs of the M_x and M_y planes for other materials of the Cu_2SnS_3 family. It is obvious to see that all the members have MCN = 1 for the M_y plane, but for the M_x plane, except for Cu_2SnS_3, all the other members have MCN = 1. This is a very different phenomenon.

APPENDIX C: THE DISTRIBUTION OF WEYL POINTS IN Cu_2SnS_3 FAMILY

In this Appendix, we give the position of Weyl points for these materials of the Cu_2SnS_3 family; see Table I and Fig. 12.

APPENDIX D: BAND STRUCTURES OF Cu_2SnS_3 FAMILY WITH HSE06

In this Appendix, we show, in Fig. 13, the band calculation results with HSE06 for all materials without SOC and partial materials with SOC.

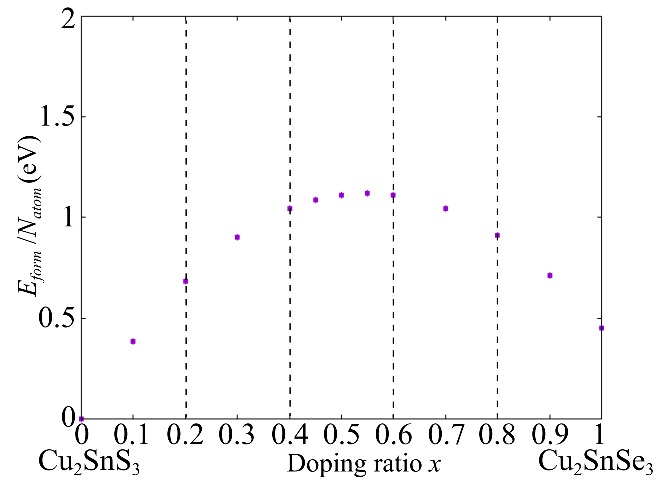

FIG. 14. The unit of formation energy as a function of the doping ratio x for $Cu_2Sn(S_{1-x}Se_x)_3$.

APPENDIX E: FORMATION ENERGY OF $Cu_2Sn(S_{1-x}Se_x)_3$

In order to study the doping ratio x dependence of the formation energy of Se-doped Cu_2SnS_3, we calculate the formation energy E_{form} by using the formula below [58,59],

$$E_{\text{form}} = E_{Cu_2Sn(S_{1-x}Se_x)_3} - E_{Cu_2SnS_3} - m\mu_{\text{Se}} + n\mu_{\text{S}}, \qquad \text{(E1)}$$

where $m = n = 3x$, and μ_{Se} and μ_{S} are the chemical potential of the isolated atom Se and S, respectively.

In practical applications, E_{form} could be averaged over all atoms (N_{atom}) as the unit of formation energy to help estimate the feasibility of practical synthesis. The unit of formation energy, $E_{\text{form}}/N_{\text{atom}}$, changes with the doping ratio x (Fig. 14). The dashed lines in Fig. 14 indicate the doping concentrations that have been synthesized experimentally [49].

[1] A. P. Schnyder, S. Ryu, A. Furusaki, and A. W. W. Ludwig, Classification of topological insulators and superconductors in three spatial dimensions, Phys. Rev. B **78**, 195125 (2008).

[2] Z. Song, T. Zhang, Z. Fang, and C. Fang, Quantitative mappings between symmetry and topology in solids, Nat. Commun. **9**, 3530 (2018).

[3] T. Zhang, Y. Jiang, Z. Song, H. Huang, Y. He, Z. Fang, H. Weng, and C. Fang, Catalogue of topological electronic materials, Nature (London) **566**, 475 (2019).

[4] M. Vergniory, L. Elcoro, C. Felser, N. Regnault, B. A. Bernevig, and Z. Wang, A complete catalogue of high-quality topological materials, Nature (London) **566**, 480 (2019).

[5] F. Tang, H. C. Po, A. Vishwanath, and X. Wan, Comprehensive search for topological materials using symmetry indicators, Nature (London) **566**, 486 (2019).

[6] Y. Xu, L. Elcoro, Z.-D. Song, B. J. Wieder, M. Vergniory, N. Regnault, Y. Chen, C. Felser, and B. A. Bernevig, High-throughput calculations of magnetic topological materials, Nature (London) **586**, 702 (2020).

[7] B. Peng, Y. Jiang, Z. Fang, H. Weng, and C. Fang, Topological classification and diagnosis in magnetically ordered electronic materials, Phys. Rev. B **105**, 235138 (2022).

[8] J. Kruthoff, J. de Boer, J. van Wezel, C. L. Kane, and R.-J. Slager, Topological Classification of Crystalline Insulators through Band Structure Combinatorics, Phys. Rev. X **7**, 041069 (2017).

[9] A. Bouhon, G. F. Lange, and R.-J. Slager, Topological correspondence between magnetic space group representations and subdimensions, Phys. Rev. B **103**, 245127 (2021).

[10] M. Z. Hasan and C. L. Kane, Colloquium: Topological insulators, Rev. Mod. Phys. **82**, 3045 (2010).

[11] X.-L. Qi and S.-C. Zhang, Topological insulators and superconductors, Rev. Mod. Phys. **83**, 1057 (2011).

[12] X. Wan, A. M. Turner, A. Vishwanath, and S. Y. Savrasov, Topological semimetal and Fermi-arc surface states in the electronic structure of pyrochlore iridates, Phys. Rev. B **83**, 205101 (2011).

[13] A. A. Burkov and L. Balents, Weyl Semimetal in a Topological Insulator Multilayer, Phys. Rev. Lett. **107**, 127205 (2011).

[14] S. M. Young, S. Zaheer, J. C. Y. Teo, C. L. Kane, E. J. Mele, and A. M. Rappe, Dirac Semimetal in Three Dimensions, Phys. Rev. Lett. **108**, 140405 (2012).

[15] C. Liu, J. Shen, J. Gao, C. Yi, D. Liu, T. Xie, L. Yang, S. Danilkin, G. Deng, W. Wang, S. Li, Y. Shi, H. Weng, E. Liu, and H. Luo, Spin excitations and spin wave gap in the ferromagnetic Weyl semimetal $Co_3Sn_2S_2$, Sci. China Phys. Mech. Astron. **64**, 217062 (2021).

[16] B.-J. Yang and N. Nagaosa, Classification of stable three-dimensional Dirac semimetals with nontrivial topology, Nat. Commun. **5**, 4898 (2014).

[17] H. Weng, C. Fang, Z. Fang, B. A. Bernevig, and X. Dai, Weyl Semimetal Phase in Noncentrosymmetric Transition-Metal Monophosphides, Phys. Rev. X **5**, 011029 (2015).

[18] H. Weng, Y. Liang, Q. Xu, R. Yu, Z. Fang, X. Dai, and Y. Kawazoe, Topological node-line semimetal in three-dimensional graphene networks, Phys. Rev. B **92**, 045108 (2015).

[19] N. P. Armitage, E. J. Mele, and A. Vishwanath, Weyl and Dirac semimetals in three-dimensional solids, Rev. Mod. Phys. **90**, 015001 (2018).

[20] H. Weng, R. Yu, X. Hu, X. Dai, and Z. Fang, Quantum anomalous Hall effect and related topological electronic states, Adv. Phys. **64**, 227 (2015).

[21] H. Weng, X. Dai, and Z. Fang, Topological semimetals predicted from first-principles calculations, J. Phys.: Condens. Matter **28**, 303001 (2016).

[22] H. Weng, C. Fang, Z. Fang, and X. Dai, A new member of the topological semimetals family, Natl. Sci. Rev. **4**, 798 (2017).

[23] A. Bernevig, H. Weng, Z. Fang, and X. Dai, Recent Progress in the Study of Topological Semimetals, J. Phys. Soc. Jpn. **87**, 041001 (2018).

[24] C. Fang, H. Weng, X. Dai, and Z. Fang, Topological nodal line semimetals, Chin. Phys. B **25**, 117106 (2016).

[25] S. Murakami, Phase transition between the quantum spin Hall and insulator phases in 3D: Emergence of a topological gapless phase, New J. Phys. **9**, 356 (2007).

[26] S. Murakami, S. Iso, Y. Avishai, M. Onoda, and N. Nagaosa, Tuning phase transition between quantum spin Hall and ordinary insulating phases, Phys. Rev. B **76**, 205304 (2007).

[27] S. Murakami and S.-i. Kuga, Universal phase diagrams for the quantum spin Hall systems, Phys. Rev. B **78**, 165313 (2008).

[28] S. Murakami, Gap closing and universal phase diagrams in topological insulators, Phys. E **43**, 748 (2011).

[29] R. Okugawa and S. Murakami, Dispersion of Fermi arcs in Weyl semimetals and their evolutions to Dirac cones, Phys. Rev. B **89**, 235315 (2014).

[30] S. Murakami, M. Hirayama, R. Okugawa, and T. Miyake, Emergence of topological semimetals in gap closing in semiconductors without inversion symmetry, Sci. Adv. **3**, e1602680 (2017).

[31] Y. Hu, C. Yue, D. Yuan, J. Gao, Z. Huang, Z. Fang, C. Fang, H. Weng, and W. Zhang, The evolution of Weyl nodes in Ni doped thallium niobate pyrochlore $Tl_{2-x}Ni_xNb_2O_7$, arXiv:2112.04127.

[32] K. Lohani, H. Nautiyal, N. Ataollahi, C. Fanciulli, I. Sergueev, M. Etter, and P. Scardi, Experimental and ab initio study of Cu_2SnS_3 (CTS) polymorphs for thermoelectric applications, J. Phys. Chem. C **125**, 178 (2021).

[33] S. G. Choi, J. Kang, J. Li, H. Haneef, N. J. Podraza, C. Beall, S.-H. Wei, S. T. Christensen, and I. L. Repins, Optical function spectra and bandgap energy of Cu_2SnSe_3, Appl. Phys. Lett. **106**, 043902 (2015).

[34] M. Mesbahi and M. L. Benkhedir, A DFT study of quaternary chalcogenide semiconductors $Cu_2\,ZnSnS(Se)_4$ by tran-blaha modified Becke-Johnson and Hubbard potentials, U.P.B. Sci. Bull., Ser. A **79**, 293 (2017).

[35] Y. Zhou, H. Wu, D. Wang, L. Fu, Y. Zhang, J. He, S. J. Pennycook, and L.-D. Zhao, Investigations on electrical and thermal transport properties of Cu_2SnSe_3 with unusual coexisting nanophases, Mater. Today Phys. **7**, 77 (2018).

[36] H. C. Po, A. Vishwanath, and H. Watanabe, Symmetry-based indicators of band topology in the 230 space groups, Nat. Commun. **8**, 50 (2017).

[37] Z. Song, T. Zhang, and C. Fang, Diagnosis for Nonmagnetic Topological Semimetals in the Absence of Spin-Orbital Coupling, Phys. Rev. X **8**, 031069 (2018).

[38] R. Yu, X. L. Qi, A. Bernevig, Z. Fang, and X. Dai, Equivalent expression of $\mathbb{Z}_2$ topological invariant for band insulators using the non-Abelian Berry connection, Phys. Rev. B **84**, 075119 (2011).

[39] D. Gresch, G. Autès, O. V. Yazyev, M. Troyer, D. Vanderbilt, B. A. Bernevig, and A. A. Soluyanov, Z2Pack: Numerical implementation of hybrid Wannier centers for identifying topological materials, Phys. Rev. B **95**, 075146 (2017).

[40] G. Kresse and J. Furthmüller, Efficiency of *ab initio* total energy calculations for metals and semiconductors using a plane-wave basis set, Comput. Mater. Sci. **6**, 15 (1996).

[41] P. E. Blöchl, Projector augmented-wave method, Phys. Rev. B **50**, 17953 (1994).

[42] J. P. Perdew, K. Burke, and M. Ernzerhof, Generalized Gradient Approximation Made Simple, Phys. Rev. Lett. **77**, 3865 (1996).

[43] A. A. Mostofi, J. R. Yates, Y.-S. Lee, I. Souza, D. Vanderbilt, and N. Marzari, WANNIER90: A tool for obtaining maximally-localized Wannier functions, Comput. Phys. Commun. **178**, 685 (2008).

[44] Q. Wu, S. Zhang, H.-F. Song, M. Troyer, and A. A. Soluyanov, WANNIERTOOLS: An open-source software package for novel topological materials, Comput. Phys. Commun. **224**, 405 (2018).

[45] C. L. Kane and E. J. Mele, Z_2 Topological Order and the Quantum Spin Hall Effect, Phys. Rev. Lett. **95**, 146802 (2005).

[46] L. Fu, C. L. Kane, and E. J. Mele, Topological Insulators in Three Dimensions, Phys. Rev. Lett. **98**, 106803 (2007).

[47] L. Fu and C. L. Kane, Topological insulators with inversion symmetry, Phys. Rev. B **76**, 045302 (2007).

[48] B. Q. Lv, H. M. Weng, B. B. Fu, X. P. Wang, H. Miao, J. Ma, P. Richard, X. C. Huang, L. X. Zhao, G. F. Chen, Z. Fang, X. Dai, T. Qian, and H. Ding, Experimental Discovery of Weyl Semimetal TaAs, Phys. Rev. X **5**, 031013 (2015).

[49] T. Irie, Lattice thermal conductivity of disordered alloys of ternary compound semiconductors $Cu_2(Sn, Ge)(Se, S)_3$ (Ag, Pb, Sb)Te_2, and (Ag, Sn, Sb)Te_2, Jpn. J. Appl. Phys. **5**, 854 (1966).

[50] Y. Han, Y. Liu, J. Wang, T. Yang, F. Zhou, M. Kuang, X. Wang, and G. Zhang, Strain-induced quantum phase transition

in the C_3Sc_4 monolayer: towards multiple gapless fermions, Nanoscale **13**, 9723 (2021).

[51] C. Hua, S. Li, Z.-A. Xu, Y. Zheng, S. A. Yang, and Y. Lu, Tunable topological energy bands in 2D dialkali-metal monoxides, Adv. Sci. **7**, 1901939 (2020).

[52] Y. Qian, Z. Tan, T. Zhang, J. Gao, Z. Wang, Z. Fang, C. Fang, and H. Weng, Layer construction of topological crystalline insulator LaSbTe, Sci. China Phys. Mech. Astron. **63**, 107011 (2020).

[53] Y. Xu, Z. Song, Z. Wang, H. Weng, and X. Dai, Higher-Order Topology of the Axion Insulator $EuIn_2As_2$, Phys. Rev. Lett. **122**, 256402 (2019).

[54] Y. Jiang, Z. Fang, and C. Fang, A $k \cdot p$ Effective Hamiltonian Generator, Chin. Phys. Lett. **38**, 077104 (2021).

[55] D. Gresch, Identifying topological semimetals, Ph.D. thesis, ETH Zurich, 2018, doi: 10.3929/ethz-b-000308602.

[56] T. H. Hsieh, H. Lin, J. Liu, W. Duan, A. Bansil, and L. Fu, Topological crystalline insulators in the SnTe material class, Nat. Commun. **3**, 982 (2012).

[57] T. H. Hsieh, J. Liu, and L. Fu, Topological crystalline insulators and Dirac octets in antiperovskites, Phys. Rev. B **90**, 081112(R) (2014).

[58] R. Liu, X. Zhou, F. Yang, and Y. Yu, Combination study of DFT calculation and experiment for photocatalytic properties of S-doped anatase TiO_2, Appl. Surf. Sci. **319**, 50 (2014).

[59] V. Çelik and E. Mete, Range-separated hybrid exchange-correlation functional analyses of anatase TiO_2 doped with W, N, S, W/N, or W/S, Phys. Rev. B **86**, 205112 (2012).